Escola de Primavera de Transição e Turbulência
Blumenau 2020

ABCM Associação Brasileira de Engenharia e Ciências Mecânicas

12th Spring School on Transition and Turbulence
September 21st-25th, 2020, Blumenau, SC, Brazil

EPTT-2020-0045
REACTOR FOR MULTIPHASE SOLID-FLUID REACTING FLOW

Adriano Ferreira de Mattos Silvares
Department of Chemical Engineering, University of São Paulo
adriano.silvares@usp.br
Song Won Park
Department of Chemical Engineering, University of São Paulo
sonwpark@usp.br
João Pedro Ferreira Del Pintor
Department of Chemical Engineering, University of São Paulo
joao.pintor@usp.br
Auta Narjara de Brito Soares
Department of Chemical Engineering, University of São Paulo
autanarjara@usp.br

Abstract. *In the present work, a three-phase system (liquid-vapor-solid) was studied, in which the formation of the solid gas clathrate hydrate strongly depends on the mass and heat transfer between vapor and liquid phases. Two reactor designs aiming to promote the contact between the vapor and liquid phases were analyzed and compared. The meso-mixing and micro-mixing characteristics were evaluated from chemical species phase distribution profiles for a continuous stirred tank reactor (CSTR) and static mixer equipment (NETmix®) type reactors. The simulation is done using ANSYS FLUENT™. The work evolved in progressive steps, at first the reactors geometries and meshes were built, followed by simulation with a single phase (liquid), using the Two Components Eulerian Model; here, the levels of micro and meso-mixtures were evaluated. Thereafter, gas phase was added and the momentum, heat and mass interphase transfer were evaluated. Finally, a third solid phase was included, which is formed by pseudo first-order reaction kinetics. In this case, an Eulerian-Eulerian-Eulerian Model was used. The comparison between results for both reactors shows how different reactor designs affect formation performance. The main challenges in such reactor modeling are: the fast production of solids in the reactor determining all life cycle of this solids, the solid-liquid-gas always has both mass transfer and thermodynamic chemical equilibrium to consider in the model. The interfacial phenomena also needs to be incorporated but with enough simplifications. All of these challenges are considered under the importance mechanism of micro-mixing. This paper aims to improve the understanding of the nature of interactions of flow inhomogeneity and micro-mixing with chemical reaction subjected to flow patterns of two different reactor designs.*

Keywords: *Reactor Design, CFD, Multiphase flow. Micro-mixing*

1. INTRODUCTION:

Hydrates have been known for over two centuries, research has been intensified in relation to the thermodynamics of systems, in which their formation and inhibition occurred [Hammerschmidt, 1934]. Initially, these studies aimed to avoid their formation and the consequent obstruction of production lines in the oil and gas industry. Hydrates are compounds that have a variety of applications of great industrial interests such as: natural gas production (given the large natural hydrate reserves) carbon dioxide capture and storage, gas separation, storage and transport processes and gas storage applications thermal energy [Ogunlade et. al., 2005 and Chatti et. al., 2005].

Technological challenges for the success of these applications hydrates formation/dissociation are associated with low rates of formation, low conversion and economic viability of industrial processes scale-up [Ribeiro et. al. 2008].

The thermodynamic properties of hydrate systems are crucial for all applications, as the conditions of temperature, pressure, gas and condensed phase composition and the presence of additives determine whether the system is in a condition of formation and stabilization, or of dissociation.

The kinetics of their formation/dissociation is still a challenge. Low rates of formation and conversion of hydrates, difficulties in experimental reproducibility ("memory effects" that lead to variation in nucleation induction time), local rates of mass and heat transfer, effects of additives (promoters/inhibitors) and others are to be elucidated.

Because multiphase flow processes with hydrate formation/dissociation is a problem area that is recently being exploited by means of numerical simulation [Li, P et. al. 2019], the present work aims the development comprehensive

model to be solved by CFD techniques that considers a multiphase and multicomponent system and the associated momentum, energy and mass transfer between phases. Two reactor designs were simulated to compare its meso-mixing and micro-mixing characteristics and how it affects hydrate formation performance.

2. MATERIAL AND METHODS:

The mechanistic CFD model was elaborated comprehensively increasing its complexity in successive steps. First the equipment residence time distribution was studied to evaluate the mixing characteristics and flow profiles. Second CO_2 and H_2O system was modeled and simulated to analyze interphase mass transfer phenomena based on Henry's law. Finally, CO_2 Hydrate, CO_2 and H_2O system was modeled employing a heterogeneous interphase reaction to represent the hydrate formation.

2.1 EQUIPMENTS GEOMETRY AND FINITE VOLUME DISCRETIZATION:

In order to develop models for simulation systems presented herein two reactor designs were selected: (i) a static mixer equipment and (ii) CSTR based on open literature [Costa, M. F., et. al. 2017 and Mork, M., et. al. 2002].

The NETmix® technology consists on a network of mixing chambers interconnected by transport channels. The network is built from the repetition of chamber unit cells organized in columns and rows as shown in Figure 1.

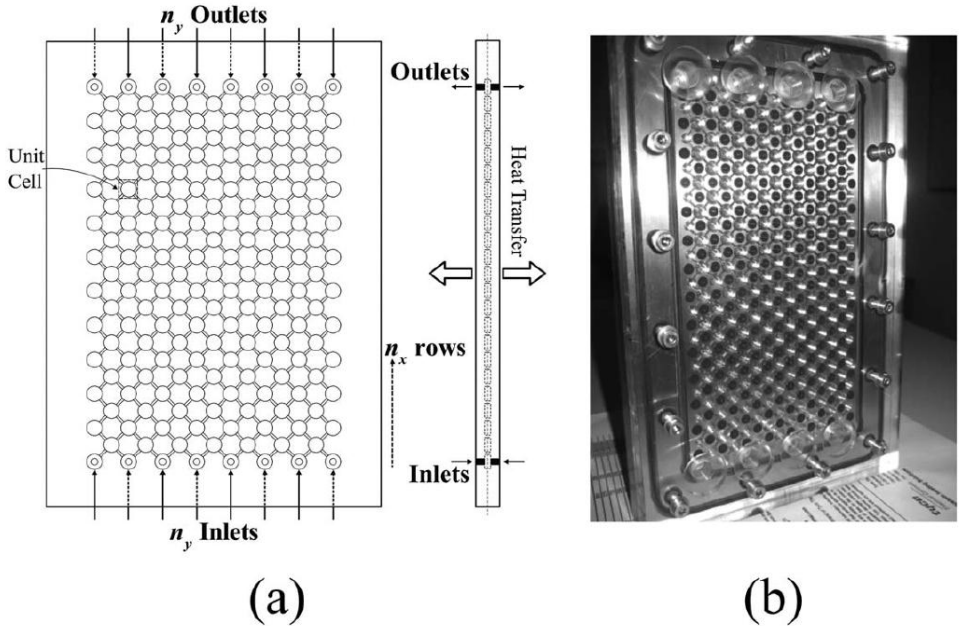

Figure 1. (a) Front and side-view drawing of a NETmix network; (b) Lab-scale NETmix. Extracted from Costa, M. F., et. al. (2017)

The continuous stirred tank reactor consists of a cylinder with inlet and outlet placed above each other. Inside the reactor four equally spaced baffles were fitted to the walls and an impeller disk with six straight blades, also called Rushton turbine, was employed to ensure agitation (Figure 2).

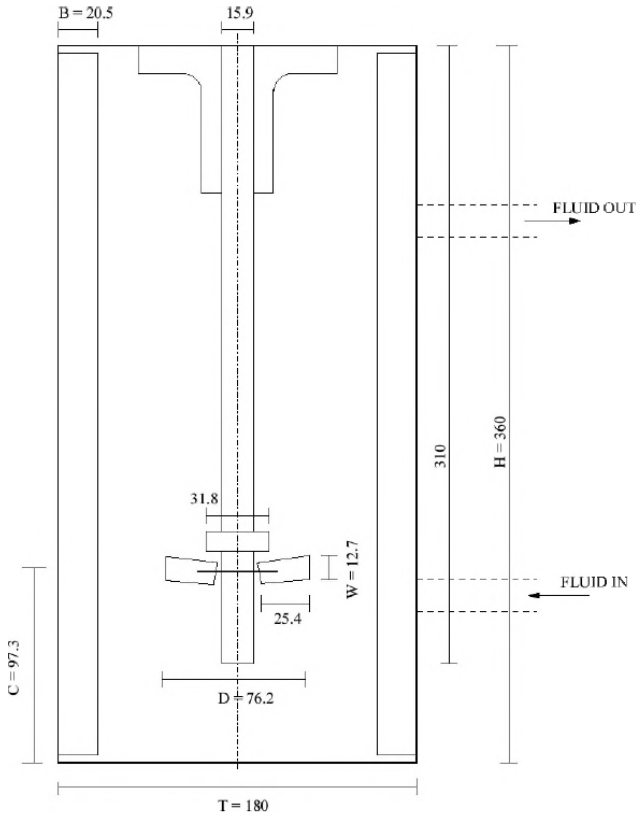

Figure 2. Inside geometry of 9.5 liter stirred tank reactor (dimensions in mm). Extracted from Mork, M. (2002)

2.1.1 NETMIX® REACTOR

Fonte et. al. (2013) developed a model aiming mitigation of computational limitations, as it is impractical to simulate the whole equipment domain. The adopted simulation strategy was based on the periodically repetitive nature of the geometry and the expected flow pattern. In his model 5 rows and 3 columns were designed, where the first and third columns are half chambers and to their outer limits, a periodic boundary condition was applied. In the present work a different approach was employed, the domain consists of 7 columns and 7 rows as shown in Figure 3 (a). No periodic boundary condition was applied. Although, due to computational limitations the whole domain (15 columns and 23 rows) was not simulated, the proposed model gives insights of the flow pattern and mixing characteristics.

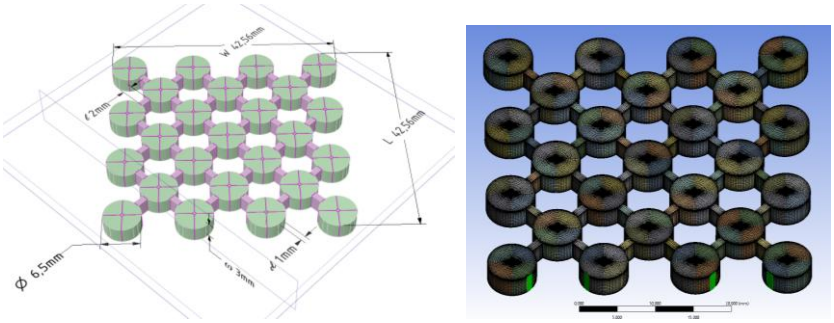

Figure 3. (a) NETmix® geometry and dimensions employed in simulations, (b) NETmix® domain mesh.

The geometry was prepared using SpaceClaim software, where the O-grid strategy [Tu, J. et. al. 2013] was selected to generate later, in ANSYS Meshing, a structured mesh presented in Figure 3 (b) which consists of 1,134,500 elements and 1,228,584 nodes. The proposed equipment total volume is equal to 2.71E-06 m^3, each chamber has a volume of 9.95E-08 m^3 and each channel has a volume of 6.07E-09 m^3.

2.1.2 CONTINUOUS STIRRED TANK REACTOR

The CSTR geometry was also prepared using SpaceClaim and its dimensions were taken from Mork, M., et. al. [2002] (see Figure 4 (a)). To solve the governing equations the inner-outer iterative procedure was used which the computational domain is subdivided in two cylindrical, non-overlapping blocks: an external, stationary block comprising the baffles, parts of the shaft, inlet and outlet openings and an inner block containing the other part of the shaft and an impeller attached to it [Montante, G. et. al. 2005]. A non-structured with 6 mm element size and 7 refinement layers applied at all baffles, shaft parts, impeller and tank walls was generated, resulting a mesh with 515,506 elements. In Figure 4 (b) the final CSTR domain mesh is presented.

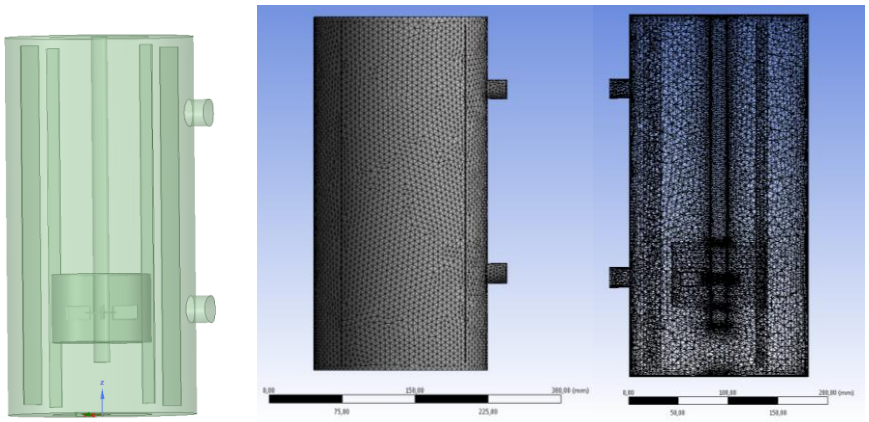

Figure 4. (a) CSTR geometry, (b) CSTR domain mesh.

3. MODELS SETUPS:

The CFD simulations of both reactors described above were performed by predictive approaches and different mathematical models. First a transient, single aqueous phase with two components model was solved to evaluate reactors characteristics of the residence time distribution (RTD), meso and micro-mixing effects. Thereafter a steady-state, two phases and two components model, based on Eulerian-Eulerian treatment of both phases was solved to evaluate momentum, heat and mass transfer between them. Finally a steady-state, three phase and two components model, on Eulerian-Eulerian-Eulerian treatment of all phases was solved to evaluate the hydrate formation kinetics.

3.1 REACTORS RESIDENCE TIME DISTRIBUTION:

Important information about the equipment hydrodynamics can be obtained analyzing its RTD. The RTD returns mixing characteristics occurring within the network (macromixing), however, it neglects the detailed information about different mixing levels (micromixing) [Laranjeira et. al. 2009].

In order to simulate the residence time distribution for the proposed equipment geometry, an isothermal single phase multicomponent transient model was developed. H_2O is the main component of the model and NaCl was selected as a tracer.

In Table 1 are presented the employed properties of the system.

Table 1. H2O and NaCl system properties.

Properties	Value	Unit
ρ (Mixture)	998.20	kg/m3
μ (Mixture)	1.00E-03	kg/m.s
Mw (H_2O)	18.00	kg/kmol
Mw (NaCl)	5.84E+04	kg/kmol

In the NETmix® reactor, once a specific channel Reynolds number is achieved, the flow inside the mixing chambers evolves to a self-sustained oscillatory laminar flow regime [Fonte, C., 2013] and therefore this regime was adopted for simulations. For the CSTR reactor flow regime is turbulent and in the present work the renormalization group (RNG) k-ε model with swirl modification was employed.

In Table 2 are presented the set of model equations numerically solved by the CFD platform. To simulate a NaCl pulse injection at equipment inlets an UDF was written and compiled, which changes the NaCl mass fraction at inlets as shown in Table 3, other boundary conditions are also presented.

Table 2. Equations employed to model equipment RTD.

Equations employed to model equipment RTD		
Continuity	$\frac{\partial \rho}{\partial t} + \nabla \cdot (\rho \vec{v}) = 0$	(1)
Momentum	$\frac{\partial (\rho \vec{v})}{\partial t} + \nabla \cdot (\rho \vec{v}\vec{v}) = -\nabla p + \nabla . \mu (\nabla \vec{v})$	(2)
Chemical species conservation	$\frac{\partial (\rho Y_i)}{\partial t} + \nabla \cdot (\vec{v} Y_i) = -\nabla \cdot \rho D_{i,m} \nabla Y_i + R_i$	(3)

(*) for turbulent flow regime $\vec{v} = \overline{\vec{v}} + \vec{v}'$, i. e. the velocity components are decomposed in mean and fluctuating velocity components. Likewise for pressure and other scalar quantities are also decomposed $\varphi = \overline{\varphi} + \varphi'$.

Table 3. Boundary conditions for RTD simulations.

Boundary	NETmix all Inlets	NETmix all Inlets	CSTR Inlets	CSTR Inlets
Simulation Time (s)	0≤ t < 2	t = 1	0≤ t < 2	t = 1
Phase	Liquid	Liquid	Liquid	Liquid
Velocity (m/s)	0.124	0.124	0.680	0.680
NaCl Mass Fraction	0	0.157	0	0.157
H_2O Mass Fraction	1	0.843	1	0.843

3.2 TWO PHASES TWO COMPONENTS SYSTEM:

Since CO_2 hydrate formation is a phenomenon that takes place at interface between different phases, it expected that the interphase mass, heat and momentum transfers play an important role. Therefore, as a second step on the modeling development, a CO_2 and H_2O system was simulated to evaluate these phenomena.

A steady-state multicomponent Euler-Euler multiphase model was developed. It was assumed that the gas phase is incompressible and there is only CO_2 at temperature and pressure of the system (5 ^oC and 32 bar). In the liquid phase, mostly composed by H_2O, dissolved CO_2 is found due to mass transfer.

In Table 4 the employed CO_2 and H_2O system properties are presented.

Table 4. CO_2 and H_2O system properties.

Properties	Value	Unit
ρ (H_2O)	998.2	kg/m^3
ρ (CO_2)@32 bar	60.61	kg/m^3
μ (H_2O)	1.00E-03	kg/m.s
μ (CO_2)	1.37E-05	kg/m.s
Mw (H_2O)	18.01	kg/kmol
Mw (CO_2)	44.01	kg/kmol
k (H_2O)	6.00E-01	w/m.K
k (CO_2)	1.45E-02	w/m.K
Cp (H_2O)	4182.00	j/kg.K

Properties	Value	Unit
Cp (CO_2)	840.37	j/kg.K
H_0 (H_2O)	-2.86E+08	j/kgmol
H_0 (CO_2)	-3.94E+08	j/kgmol
Henry's constant (CO_2 - H_2O)	3.03E+06	m^3.Pa/kgmol
Bubbles Radius (BR)	$0.01 \leq BR \leq 1$	mm

The Euler-Euler approach treats mathematically different phases as interpenetrating continua. The volume of a phase cannot be occupied by the other phases; therefore the concept of phase volume fraction is applied. Volume fractions are assumed to be continuous functions of space and time and their sum is equal to one (Equation (5)).

The volume fraction and mass conservation of each phase is calculated by the continuity equation. A set of n continuity (Equation (7)) and momentum (Equation (8)) equations are solved for each phase and coupling is achieved through pressure and interphase exchange coefficients [ANSYS Fluent Theory Guide, 2020].

In the present work it was assumed that momentum equations is a function of the phase apparent viscosity (λ_q) and shear stress viscosity (μ_q), stress strain tensor, lift forces ($\vec{F}_{lift,q}$), virtual mass force ($\vec{F}_{vm}$), wall lubrication force ($\vec{F}_{wl,q}$) interphase interaction forces ($\vec{R}_{pq}$ Equation (10)) and the velocity of each phase.

In order to predict the mass, momentum and energy transfers through the interface between phases, the interfacial area concentration (IAC) is an important parameter. For the CO2 and H2O system an IAC transport equation was solved enabling the prediction of bubble diameter distribution considering nucleation rate, coalescence and breakage effects (Equation (11)). The interfacial area concentration ($\chi_p = A_i$) has m^2/m^3 unit and α_{dp} is the discrete phase volume fraction. The two terms on right hand side of Equation (11) represent the bubble expansion due to compressibility and chemical specie phase mass transfer. $\dot{m}_{dp}$ is the mass transfer rate into the gas phase per unit mixture volume. S_{RC} and S_{TI} are the coalescence sink term due to random collision and breakage source term due to turbulent impact, which the Hibiki-Ishii [2000] model were adopted. It can be noticed that the interphase interaction forces are directly dependent on the momentum transfer coefficient (Equation (15)), which in turns depends on A_i, on drag function(f Equation (17)) and on "particulate relaxation time"(τ_p Equation (16)). Nearly all definitions of f include a drag coefficient (C_D Equation (20)) that is based on the relative Reynolds number (Re) and in this work the Schiller and Naumann model was selected [Schiller, L.; et. al., 1935].

For multiphase flows, the effect of lift forces ($\vec{F}_{lift,q}$) on the secondary phase occurs due to velocity gradients in the primary-phase flow field. From Drew [1993], the lift force acting on a secondary phase p in a primary phase q can be calculated by Equation (21), which is dependent of the lift coefficient (C_l). In order to calculate the lift coefficient the Legendre-Magnaudet [Legendre, D.; et. al. 1998] model was selected, since it is applicable to small diameter spherical fluid particles.

The virtual mass effect occurs when a secondary phase p accelerates relative to the primary phase q. The inertia of the primary phase mass experienced by the accelerating particles (bubbles) exerts a virtual mass force on them and this force can be calculated by Equation (27).

For liquid-gas flow the effect of wall lubrication forces on the secondary phase push it away from walls. The wall lubrication force acting on a secondary phase, p, in primary phase, q, has general form of Equation (30) and is dependent on the wall lubrication coefficient (C_{wl}). The adopted model for C_{wl} calculation was proposed by Antal et. al. [1991].

For multiphase energy conservation balance, enthalpy equations for each phase are solved and phase interactions are accounted. Equation (37) shows the general form of phase energy conservation. The internal energy balance for phase q is written in terms of phase enthalpy (Equation (33)). The volumetric rate of energy transfer between phases, Q_{pq} (Equation (34)), is a function of the temperature difference, the interfacial area, A_i and the volumetric heat transfer coefficient (h_{pq} Equation (35)) between phases p and q and accounts for convection mechanism between phases. To compute the Nusselt number, necessary to calculate h_{pq}, Ranz and Marshall Correlation was applied (Equation (36)) [Ranz, W. E., et. al.; 1952]. The heat flux $\vec{q}_q$ is accounted for conduction heat transfer mechanism and the energy transfer due to chemical species phase changes from p to q.

To model interphase species mass transfer, phase species transport equation are solved along with the phase mass, momentum and energy equations. The transport equation for the local mass fraction Y_q^i of specie i in phase q, among n phases, is given by Equation (38). The mass transfer source from species j on phase p to species i on phase q is accounted by $\dot{m}_{p^i q^j}$ term given by Equation (39). Note that species j and i are the same chemical species, however in different phases.

In the present work the two resistance interphase mass transfer model [Whitman, W. G.; 1923] was applied. It considers that the specie transport resistance from the bulk volume of a fluid to the interface phase q and from the interface of the phase *p* to its bulk volume is diffusion controlled. Therefore within each phase of a system the volumetric rates of phase mass exchange can be expressed by Equations (40) phase *q* and (41) phase *p* and are dependent on interface and bulk concentration of the specie. The phase mass transfer coefficient, k_q and k_p, are defined on either side of the phase interface and was modeled as a function of the phase Sherwood number for the liquid phase and as zero resistance for the gas, since the bulk and interface concentration are the same, $k_p \to \infty$.

Through the interface the transport is instantaneous and the species are in dynamic equilibrium between the phases, which is described by Henry's law given by Equation (48).

In Table 5 the model equations used to describe the CO_2 and H_2O are presented.

Table 5. CO_2 and H_2O model equations.

CO_2 and H_2O system model equations		
Phase volume	$V_q = \int_V \alpha_q dV$	(4)
Volume fraction	$\sum_{q=1}^{n} \alpha_q = 1$	(5)
Phase effective density	$\hat{\rho}_q = \alpha_q \rho_q$	(6)
Continuity	$\frac{\partial}{\partial t}(\alpha_q \rho_q) + \nabla(\alpha_q \rho_q \vec{v}_q) = \sum_{p=1}^{n}(\dot{m}_{pq} - \dot{m}_{qp}) + S_q$	(7)
Momentum	$\frac{\partial}{\partial t}(\alpha_q \rho_q \vec{v}_q) + \nabla(\alpha_q \rho_q \vec{v}_q \vec{v}_q) = -\alpha_q \nabla p + \nabla . \bar{\bar{\tau}}_q + \alpha_q \rho_q \vec{g} + \sum_{p=1}^{n}(\vec{R}_{pq} + \dot{m}_{pq}\vec{v}_{pq} - \dot{m}_{qp}\vec{v}_{qp}) + (\vec{F}_{lift,q} + \vec{F}_{vm,q} + \vec{F}_{wl,q})$	(8)
Stress strain tensor	$\bar{\bar{\tau}}_q = \alpha_q \mu_q (\nabla \vec{v}_q + \nabla \vec{v}_q^T) + \alpha_q \left(\lambda_q - \frac{2}{3}\mu_q\right) \nabla . \vec{v}_q \bar{\bar{I}}$	(9)
Interphase interaction forces	$\sum_{p=1}^{n} \vec{R}_{pq} = \sum_{p=1}^{n} K_{pq}(\vec{v}_p - \vec{v}_q)$	(10)
Interphase area density symmetric model	$\frac{\partial(\rho_{dp}\chi_p)}{\partial t} + \nabla . (\rho_{dp}\vec{u}_{dp}\chi_p) = \frac{1}{3}\frac{D\rho_{dp}}{Dt}\chi_p + \frac{2}{3}\frac{\dot{m}_{dp}}{\alpha_{dp}} + \rho_{dp}(S_{RC} + S_{TI})$	(11)
Bubble coalescence sink term	$s_{RC} = -\frac{\Gamma_c}{\psi^{11/3}} \frac{\epsilon^{1/3}}{(\alpha_{dpmax} - \alpha_{dp})} \alpha_{dp}^{1/3} \chi_p^{5/3} \exp\left[-K_c \psi^{5/6} \frac{\rho_f^{1/2} \epsilon^{1/3}}{\sigma^{1/2}} \left(\frac{\alpha_{dp}}{\chi_p}\right)^{5/6}\right]$	(12)
Averaged bubble size	$d_b = \psi \frac{\alpha_{dp}}{\chi_p}$	(13)
Bubble breakage source term	$s_{TI} = -\frac{\Gamma_B}{\psi^{11/3}} \frac{(1-\alpha_{dp})\epsilon^{1/3}\chi_p^{5/3}}{\alpha_{dp}^{2/3}(\alpha_{dpmax} - \alpha_{dp})} \alpha_{dp}^{1/3} \chi_p^{5/3} \exp\left[-\frac{K_B}{\psi^{5/3}} \frac{\sigma}{\rho_f^{1/2} \epsilon^{2/3}} \left(\frac{\chi_p}{\alpha_{dp}}\right)^{5/3}\right]$	(14)
Momentum transfer coefficient	$K_{pq} = \frac{\rho_p f}{6\tau_p} d_p A_i$	(15)
Particulate relaxation time	$\tau_p = \frac{\rho_p d_p^2}{18\mu_p}$	(16)
Drag function	$f = \frac{C_D Re}{24}$	(17)
Relative Reynolds number	$Re = \frac{\rho_q \lvert\vec{v}_p - \vec{v}_q\rvert d_p}{\mu_q}$	(18)
Mixture viscosity	$\mu_q = \alpha_p \mu_p + \alpha_q \mu_q$	(19)
Drag coefficient	$C_D = \frac{24}{Re}(1 + 0.1Re^{0.687})$	(20)

CO_2 and H_2O system model equations		
Lift force	$\vec{F}_{lift} = -C_l \rho_q \alpha_p (\vec{v}_q - \vec{v}_p) \times (\nabla \times \vec{v}_q)$	(21)
Vorticity Reynolds number	$Re_\omega = \frac{\rho_q \lvert \nabla \times \vec{v}_q \rvert {d_p}^2}{\mu_q}$	(22)
Saffman-Mei model parameters	$\beta = 0.5 \left({Re_\omega}/{Re_p} \right), Sr = 2\beta$	(23)
Lift force coefficient	$C_l = \sqrt{(C_{l,lowRe})^2 + (C_{l,highRe})^2}$	(24)
Low Reynolds lift force coefficient	$C_{l,lowRe} = \frac{6}{\pi^2} (Re_p Sr)^{-0.5} \frac{2.55}{\left(1 + 0.2 \frac{Re_p}{Sr}\right)^{1.5}}$	(25)
Low Reynolds lift force coefficient	$C_{l,highRe} = \frac{1}{2} \frac{1 + 16 {Re_p}^{-1}}{1 + 29 {Re_p}^{-1}}$	(26)
Virtual mass force	$\vec{F}_{vm} = C_{vm} \rho_q \alpha_p \left(\frac{d_q \vec{v}_q}{dt} - \frac{d_p \vec{v}_p}{dt} \right)$	(27)
Virtual mass coefficient	$C_{vm} = 0.5$	(28)
Phase material time derivative	$\frac{d_q(\varphi)}{dt} = \frac{d_q(\varphi)}{dt} + (\vec{v}_q . \nabla)\varphi$	(29)
Wall lubrication force	$\vec{F}_{wl,q} = C_{wl} \rho_q \alpha_p \lvert (\vec{v}_q - \vec{v}_p) \rvert^2 \vec{n}_w$	(30)
Wall lubrication coefficient	$C_{wl} = \max\left(0, \frac{C_{w1}}{d_b} + \frac{C_{w2}}{y_w}\right)$; $C_{w1} = -0.01$ and $C_{w2} = 0.05$	(31)
Distance to the nearest wall	$y_w \leq -\left({C_{w2}}/{C_{w1}} \right) d_p$	(32)
Phase enthalpy	$H_q = \int C_{p,q} dT_q$	(33)
Volumetric rate of energy transfer	$Q_{pq} = h_{pq} A_i (T_p - T_q)$	(34)
Volumetric heat transfer coefficient	$h_{pq} = \frac{k_q Nu_p}{d_p}$	(35)
Energy	$\frac{\partial}{\partial t}(\alpha_q \rho_q h_q) + \nabla(\alpha_q \rho_q \vec{v}_q h_q) = \alpha_q \frac{dp_q}{dt} - \nabla . \vec{q}_q + \sum_{p=1}^{n} (Q_{pq} + \dot{m}_{pq} h_{pq} - \dot{m}_{qp} h_{qp})$	(36)
Nusselt number	$Nu_p = 2 + 0{,}6 {Re_p}^{1/2} {Pr}^{1/3}$	(37)
Prandtl number	$Pr = \frac{Cp_q \mu_q}{\kappa_q}$	(38)
Mass fraction of species i in phase q	$\frac{\partial (\alpha_q \rho_q Y_q^i)}{\partial t} + \nabla \cdot (\alpha_q \rho_q \vec{v}_q Y_q^i) = -\nabla \cdot (\alpha_q \vec{j}_q^i) + \sum_{p=1}^{n} \dot{m}_{p^i q^j}$	(39)
Volumetric rate of species mass transfer	$\dot{m}_{p^i q^j} = k_{pq} A_i \left(K^{\rho}_{q^i p^j} \rho_p^j - \rho_q^i \right)$	(40)
Volumetric rates of phase q mass exchange	$\dot{m}_{q^i} = k_q A_i (\rho_{q,s}^i - \rho_q^i)$	(41)
Volumetric rates of phase p mass exchange	$\dot{m}_{p^j} = k_p A_i (\rho_{p,s}^j - \rho_p^j)$	(42)
Dynamic equilibrium condition on phase interface	$\dot{m}_{q^i} + \dot{m}_{p^j} = 0$	(43)
Concentration relations	$\rho_q^i = M^i C_q^i$; $X_q^i = \frac{C_q^i}{C_q}$; $Y_q^i = \frac{\rho_q^i}{\rho_q}$	(44)

CO_2 and H_2O system model equations		
General form of equilibrium ratios for mass concentration	$K^{\rho}_{q^i p^j} = \frac{\rho^i_q}{\rho^j_p}$	(45)
Henry's law	$P^j_p = H^x X^i_{q,e}$	(46)
Dalton's law	$P^i_p = X^j_{p,e} P$	(47)
Henry's law equilibrium ratio	$K^x_{q^i p^j} = \frac{P}{H^x}$	(48)

(*) for turbulent flow regime $\vec{v} = \overline{\vec{v}} + \vec{v}'$, i. e. the velocity components are decomposed in mean and fluctuating velocity components. Likewise for pressure and other scalar quantities are also decomposed $\varphi = \overline{\varphi} + \varphi'$.

As initial condition for the system, the equipment was considered to be filled only with water. The gravity force was activated aiming the future simulation with solids. An operational pressure of 32 bar was defined. The equipment walls were set as non-slip boundaries with fixed temperature of 5 ^oC. The applied simulation boundary conditions are presented in Table 6.

Table 6. Boundary conditions for CO_2 and H_2O

Boundary	NETmix Inlet1/Inlet3	NETmix Inlet2/Inlet4	CSTR Inlet
Phase	Aqueous	Gas	Aqueous and Gas
Gas Phase Velocity (m/s)	0	0.277	1.590
Aqueous Phase Velocity (m/s)	0.124	0	0.680
CO_2 Gas Phase Mass Fraction	0	1	1
H2O Aqueous Phase Mass Fraction	1	0	1
Gas Phase Volume Fraction	0	1	0.7
Aqueous Phase Volume Fraction	1	0	0.3
Temperature (^oC)	5	5	5
IAC (m-1)	0.0001	0.0001	0.0001

3.3 THREE PHASES TWO COMPONENTS SYSTEM:

In order to model the CO_2 hydrate, CO_2 and H_2O system the same set of model equations applied for CO_2 and H_2O system were applied, however, due to the third (solid) phase formation some additional considerations must be observed and extra set of model equations were solved.

Gas clathrates hydrates are known as a non-stoichiometric formation phenomenon, therefore some of hydrate cages may be or not occupied by gas molecules. In this work the CO_2 hydrate were considered to be an ideal clathrate hydrate formation phenomenon, which follows the stoichiometry given by Reaction (R.1). Furthermore, it was assumed that the hydrate formation takes place when dissolved CO_2 in liquid phase are encaged by water molecules resulting the solid hydrate phase.

$$8CO_2 + 46H_2O \rightarrow 8CO_2.46H_2O\ (CO_2\ Hydrate) \quad \text{(R.1)}$$

Since, the hydrate formation phenomenon is assumed to take place from CO_2 and H_2O present in the liquid phase, which leads to as solid phase formation, the momentum, energy and mass balance for solid and liquid phases must

account for the sources of momentum, $S_q^{\vec{v}}$ (Equations (49) and (53)), enthalpy, S_q (Equations (55)), and mass, $\mathcal{R}$ (Equations (57) and (58)) and for the gas phase the equations presented in Table 5 remain valid as well as the continuity equation employed for CO_2 and H_2O system, which is valid for all phases (Equations (7)).

The momentum equation for solid phase uses a multi-fluid granular model to describe the flow behavior of a fluid-solid mixture. The solid-phase stresses are derived by making an analogy between the random particle motion arising from particle-particle collisions and the thermal motion of molecules in a gas, taking into account the inelasticity of the granular phase. As is the case for a gas, the intensity of the particle velocity fluctuations determines the stresses, viscosity, and pressure of the solid phase. The kinetic energy associated with the particle velocity fluctuations is represented by granular temperature which is proportional to the mean square of the random motion of particles [ANSYS Fluent Theory Guide, 2020]. The solids stress tensor contains shear and bulk viscosities arising from particle momentum exchange due to translation and collision. A frictional component of viscosity can also be included to account for the viscous-plastic transition that occurs when particles of a solid phase reach the maximum solid volume fraction (Equation (50). For collisional and kinetic viscosities the model proposed by Gidaspow, D. et. al. [1992] was selected. To calculate the solid bulk viscosity that accounts for the resistance of the granular particles to compression and expansion the Lun C., et al. [1984] model was chosen. For frictional viscosity the Schaeffer [1987] model was selected which depends on the friction pressure that was calculated based on Syamlal, M., [1993] work. The granular temperature for solids phase is proportional to the kinetic energy of the particles' random motion and is formally expressed by Equation (51), and is calculated based on algebraic formulation (Equation (52))

Forces that act on solid phase were assumed to be the same as for gas phase, except wall lubrication forces, which is a phenomenon valid for bubbles flowing in the liquid phase. Therefore, the momentum balances for the solid and liquid phases are described by Equations (57), and (53) and the gas phase remain the same as presented in Table 5.

The interfacial area density (A_i), was calculated by Equation (54) for the hydrate phase. Besides the above mentioned models, other models and correlations used to close momentum balance of solid phase are presented in Table 5 and were employed for all phases.

CO_2 hydrate formation phenomenon was treated as a heterogeneous reaction with a pseudo-first order kinetics in respect to CO_2 concentration in liquid phase (Equation (59)). Based on this formation rate kinetics the source terms $S_q^{\vec{v}}$, S_q and $\mathcal{R}$ can be computed. The simulation were carried out with a kinetic rate constant k = 1.75 s^{-1} [Li, P., 2019].

For the momentum transfer between liquid and solid phases it is assumed that the hydrate takes the momentum from H_2O and dissolved CO_2 in liquid phase in the ratio of it formation rate. Hence, the hydrate forming molecules net velocity is calculated (Equation (60)) and the source terms for solid and liquid phase are computed (Equations (61) and (62)).

Similarly, to calculate energy transfer between phases the net enthalpy of hydrate forming molecules is first computed by means of their formation enthalpy and the species enthalpy in the liquid phase (Equation (63)) and then the enthalpy source terms for solid and liquid phase (Equation (64) and (65)). According to Sloan et. al. [2007] the CO_2 hydrate dissociation enthalpy is 65.22 kj/mol, in order to match this value the CO2 hydrate enthalpy of formation was adjusted and CO_2 and H_2O enthalpy of formation were taken from Fluent component data base library, the system properties employed in the simulations are presented in Table 8.

The mass transfer between liquid and solid phases due to the hydrate formation phenomenon is calculated by Equations (66) and (67).

In Table 7 is presented the summary of equation employed to model CO_2 Hydrate, CO_2 and H_2O system.

For this system model simulation, the initial condition was the equipment filled only with H_2O at 5 ^oC. Same operational pressure and walls boundary conditions applied to previous system were used. The other boundary conditions are presented in Table 9.

Table 7. CO2 Hydrate, CO2 and H2O system model equations

CO_2 Hydrate, CO_2 and H_2O system model equations		
Momentum solid phase	$\frac{\partial}{\partial t}(\alpha_s\rho_s\vec{v}_s) + \nabla(\alpha_s\rho_s\vec{u}_s\vec{u}_s) = -\alpha_s\nabla p - \nabla p_s + \nabla.\bar{\bar{\tau}}_s + \alpha_s\rho_s\vec{g} + \sum_{p=1}^{n}(\vec{R}_{sq}) + (\vec{F}_{lift,s} + \vec{F}_{vm,s}) + S_{qs}^{\vec{v}}$	(49)
Solids shear viscosity	$\mu_s = \mu_{s,col} + \mu_{s,kin} + \mu_{s,fr}$	(50)
Granular temperature	$\Theta_s = \frac{1}{3}u_{s,i}u_{s,i}$	(51)
Granular temperature transport equation	$\frac{3}{2}\frac{\partial}{\partial t}(\rho_s\alpha_s\Theta_s) = (-p_s\bar{\bar{I}} + \bar{\bar{\tau}}_s) : \nabla\vec{u}_s - \gamma_{\Theta_s} + \varphi_{ls}$	(52)
Momentum liquid phase	$\frac{\partial}{\partial t}(\alpha_q\rho_q\vec{v}_q) + \nabla(\alpha_q\rho_q\vec{v}_q\vec{v}_q) = -\alpha_q\nabla p + \nabla.\bar{\bar{\tau}}_q + \alpha_q\rho_q\vec{g} + \sum_{p=1}^{n}(\vec{R}_{pq} + \dot{m}_{pq}\vec{v}_{pq} - \dot{m}_{qp}\vec{v}_{qp}) + (\vec{F}_{lift,q} + \vec{F}_{vm,q} + \vec{F}_{wl,q}) + S_q^{\vec{v}}$	(53)
Interphase area density particle model	$A_i = \frac{6\alpha_p}{d_p}$	(54)
Energy solid phase	$\frac{\partial}{\partial t}(\alpha_q\rho_q h_q) + \nabla(\alpha_q\rho_q\vec{u}_q h_q) = \alpha_q\frac{dp_q}{dt} - \nabla.\vec{q}_q + S_q + \sum_{p=1}^{n}(Q_{pq})$	(55)
Energy liquid phase	$\frac{\partial}{\partial t}(\alpha_q\rho_q h_q) + \nabla(\alpha_q\rho_q\vec{v}_q h_q) = \alpha_q\frac{dp_q}{dt} - \nabla.\vec{q}_q + S_q + \sum_{p=1}^{n}(Q_{pq} + \dot{m}_{pq}h_{pq} - \dot{m}_{qp}h_{qp})$	(56)
Mass fraction of species i in phase solid phase	$\frac{\partial(\alpha_q\rho_q Y_q^i)}{\partial t} + \nabla\cdot(\alpha_q\rho_q\vec{u}_q Y_q^i) = -\nabla\cdot(\alpha_q\vec{J}_q^i) + \mathcal{R}$	(57)
Mass fraction of species i in phase liquid phase	$\frac{\partial(\alpha_q\rho_q Y_q^i)}{\partial t} + \nabla\cdot(\alpha_q\rho_q\vec{v}_q Y_q^i) = -\nabla\cdot(\alpha_q\vec{J}_q^i) + \sum_{p=1}^{n}\dot{m}_{p^i q^j} + \mathcal{R}$	(58)
Hydrate formation rate kinetics	$r = \frac{d[CO_2]}{dt} = k\left(\frac{Y_q^i\rho_q\alpha_q}{MW_{iq}}\right)$	(59)
Hydrate forming molecules net velocity	$\vec{v}_{net} = \frac{46MW_{H_2O}\vec{v}_q + 8MW_{CO_2}\vec{v}_q}{46MW_{H_2O} + 8MW_{CO_2}}$	(60)
Solid phase momentum source term	$S_s^{\vec{v}} = r\vec{v}_{net}(MW_{CO_2Hydrate}\vec{u}_q)$	(61)
Liquid phase momentum source term	$S_l^{\vec{v}} = -r(46MW_{H_2O}\vec{v}_q + 8MW_{CO_2}\vec{v}_q)$	(62)
Hydrate forming molecules net enthalpy	$H_{net} = \frac{46MW_{H_2O}(H_{H_2O} + h_{H_2O}^f) + 8MW_{CO_2}(H_{CO_2} + h_{CO_2}^f)}{46MW_{H_2O} + 8MW_{CO_2}}$	(63)
Solid phase energy source term	$S_s = rH_{net}(MW_{CO_2Hydrate} - MW_{CO_2Hydrate}h_{CO_2Hydrate}^f)$	(64)
Liquid phase energy source term	$S_l = -r(46MW_{H_2O}H_{H_2O} + 8MW_{CO_2}H_{CO_2})$	(65)
Solid phase mass source term	$\mathcal{R}_s = r(MW_{CO_2Hydrate})$	(66)
Liquid phase mass source term	$\mathcal{R}_l = -r(46MW_{H_2O} + 8MW_{CO_2})$	(67)

(*) for turbulent flow regime $\vec{v} = \overline{\vec{v}} + \vec{v}'$, i. e. the velocity components are decomposed in mean and fluctuating velocity components. Likewise for pressure and other scalar quantities are also decomposed $\varphi = \overline{\varphi} + \varphi'$.

Table 8. CO_2 Hydrate, CO_2 and H_2O system properties.

Properties	Value	Unit
ρ (H_2O)	998.20	kg/m^3
ρ (CO_2 Hydrate)	1120.00	kg/m^3
ρ (CO_2)@32 atm	60.61	kg/m^3
μ (H_2O)	1.00E-03	kg/m.s
μ (CO_2 Hydrate)	3.5E-03	kg/m.s
μ (CO_2)	1.37E-05	kg/m.s
Mw (H_2O)	1.80E+01	kg/kmol
Mw (CO_2 Hydrate)	1.18E+03	kg/kmol
Mw (CO_2)	4.40E+01	kg/kmol
k (H_2O)	0.60	w/m.K
k (CO_2 Hydrate)	0.57	w/m.K
k (CO_2)	1.45E-02	w/m.K
Cp (H_2O)	4182.00	j/kg.K
Cp (CO_2 Hydrate)	2.03	j/kg.K
Cp (CO_2)	840.37	j/kg.K
H_0 (H_2O)	-2.86E+08	j/kgmol
H_0 (CO_2 Hydrate)	-1.64E+10	j/kgmol
H_0 (CO_2)	-3.94E+08	j/kgmol
CO_2 Hydrate formation ΔH	-6.52E+07	j/kgmol
Henry's constant (CO_2-H_2O)	3.03E+06	m^3.Pa/kgmol
Bubbles Radius (BR)	$0.01 \leq BR \leq 1$	mm
CO_2 Hydrate Radius	0.01	mm

Table 9. CO_2 Hydrate, CO_2 and H_2O system applied boundary conditions.

Boundary	NETmix Inlet1/Inlet3	NETmix Inlet2/Inlet4	CSTR Inlet	(NETmix and CSTR) All Inlets
Phase	Aqueous	Gas	Aqueous and Gas	Solid
Gas Phase Velocity (m/s)	0	0.277	1.59	0
Aqueous Phase Velocity (m/s)	0.124	0	0.68	0
CO_2 Gas Phase Mass Fraction	0	1	1	0
H_2O Aqueous Phase Mass Fraction	1	0	1	0
Gas Phase Volume Fraction	0	1	0.7	0
Aqueous Phase Volume Fraction	1	0	0.3	
Temperature (^{o}C)	5	5	5	0
IAC (m^{-1})	0.0001	0.0001	0.0001	0.0001

4. RESULTS AND DISCUSSION:

The purpose of this work is to model and compare simulation results of two different reactor designs employed for gas clathrate hydrates production from the various fluid dynamics mechanistic perspectives. Starting from the micro and meso-mixing characteristics analysis, through phase equilibrium mass transfer mechanism, to CO_2 hydrate formation phenomenon and its implications on the equipments hydrodynamics.

4.1 REACTORS RESIDENCE TIME DISTRIBUTION:

The residence time distribution (RTD) measures features of ideal or non-ideal flows associated with the bulk flow patterns or macro-mixing in equipments. The micro-mixing term is the spatial mixing at the molecular scale that is bounded, but not determined solely by the residence time distribution. These bounds are extreme conditions known as complete segregation and maximum mixedness. Those represent, respectively, the least and most molecular-level mixing that is possible for a given residence time distribution [Paul, E. L.; 2004]. Knowing the equipment RTD it is possible to evaluate a first order, isothermal and homogeneous reaction yields, because it depends only on the time that a molecule has spent in the system and not on interactions or mixing with other molecules. Two extreme hypothetical conditions are considered for continuous stirred tank reactor (CSTR) model; the local segregation, which there is no mixing between molecules entering the system at different times and the micro-mixing maximum mixedness, which is the highest amount of molecular mixing. Yields calculations for these hypothetical conditions are the limits and the yield for a real system will usually lie within them. Therefore the knowledge of equipment RTD gives important insights on its design and operational conditions (e.g. fouling, temperature measurements and geometrical characteristics). Hence, the CFD simulation of current equipment RTD was carried out employing H_2O and NaCl as tracer.

Since for NETmix® reactor simulated geometry the total volume V_t = 2.71E-06 m^3 and the total volumetric flow rate q_t = 3.72E-07 m^3/s was applied as boundary condition, the mean residence time $\tau = {}^{V_t}/_{q_t}$ is 6.8 s and for CSTR reactor V_t = 9.50 m^3 and q_t = 3.33E-04 m^3/s, the mean residence time $\tau = {}^{V_t}/_{q_t}$ is 28.8 s. However, the simulation results show that the residence times for NaCl to be fully washed out from NETmix® and CSTR are about 11 s and 180 s respectively.

Since the mean residence time for the reactor designs are more than four orders of magnitude different, RTDs results are presented in Figure 5 in terms of normalized average NaCl mass fraction at outlets as a function normalized time.

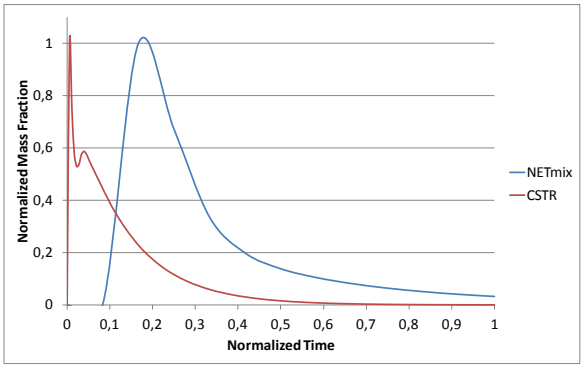

Figure 5. NETmix® and CSTR residence time distributions.

The NaCl mass fraction pulse injection boundary condition for both reactors designs is exactly the same. After NaCl pulse, traces of NaCl at CSTR reactor outlet are very quickly noticed, while for NETmix® reactor it takes some time for first NaCl traces to reach the outlets. Also for the CSTR the flow pattern leads to NaCl concentration inhomogeneities and a second peak in the RTD is observed. On the other hand, for NETmix® flow pattern results more homogeneous NaCl concentration distribution leading to a single peak RTD. Furthermore in NETmix® NaCl spends relatively more time to be washed out than the CSTR reactor.

In Figure 6 reactors velocities profiles show that CSTR reactor has a preferential path driving the flow to enter and leave it quickly, while NETmix® enables the flow to experience all chambers with similar velocities providing an intensified mixing characteristics.

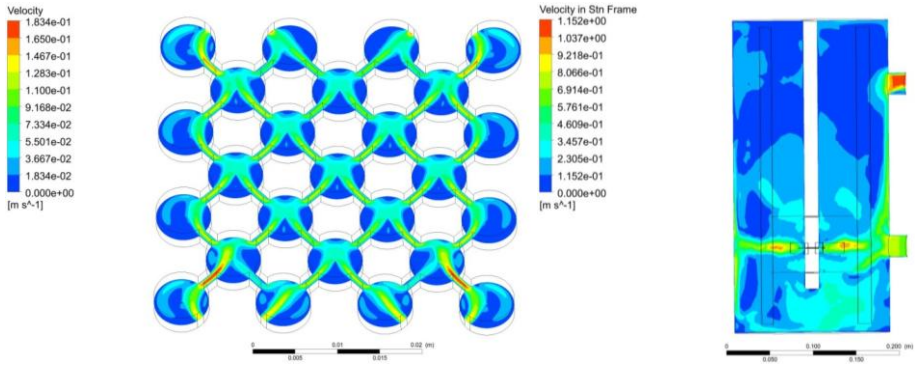

Figure 6. (a) NETmix® and (b) CSTR velocity profiles.

4.2 TWO PHASES TWO COMPONENTS SYSTEM:

There are many processes in which gas–liquid contacting is important. In the case of CO_2 hydrate formation, the gas phase must be effectively and efficiently contacted with liquid to provide mass transfer through absorption leading to chemical conditions for its formation.

Usually, turbulent flow regime is employed due to mass interchange in both radial and axial direction promoted by turbulent eddies. In laminar, steady, non-chaotic flows the velocity vectors are parallel and there is no radial mixing. The action of diffusion is minimal leading to a very long mixing time. However, static mixers are effective devices in laminar flow regime. In this sense the proposed static mixer (NETmix®) and the CSTR reactors were simulated to compare the mixing and mass transfer characteristics. The simulations were carried out in steady-state conditions using the pseudo transient solution method.

Reactor designs micro-mixing characteristics are presented in terms of liquid and gas phase volume fraction profiles shown in Figure 7 and 8. For the static mixer reactor maximum micro-mixing is observed in two middle columns, which receive more symmetrical distribution of gas and liquid streams and molecular diffusion of the gas phase and CO_2 dissolved in aqueous phase are remarkably pronounced. The stretching and folding pattern created by the channel-chamber arrangement promote this effect, since the flow is accelerated through the channels and slow down in the chambers (see Figure 6), while for the CSTR reactor the micro-mixing occurs mainly near reactor inlet and impeller walls, where the gas phase and CO_2 dissolved in aqueous phase diffuse in approximately time the energy of eddies of Kolmogorov size (η) take to dissipate (Batchelor scale, λ_B).

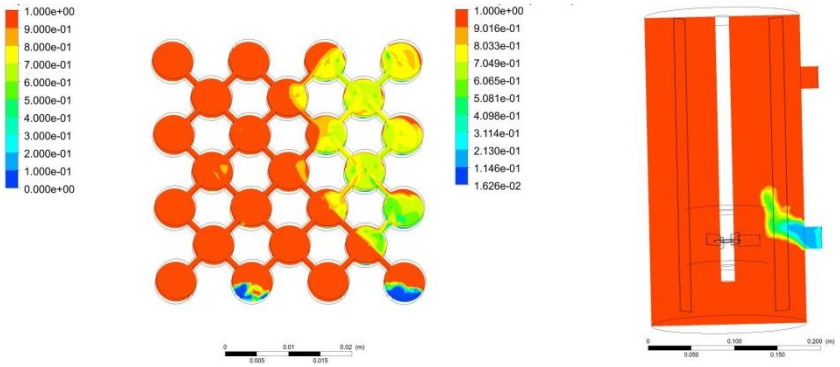

Figure 7. (a) NETmix® and (b) CSTR aqueous phase volume fraction profiles.

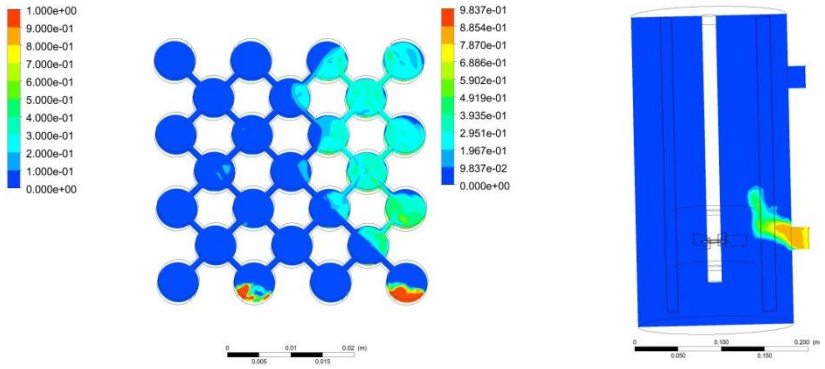

Figure 8. (a) NETmix® and (b) CSTR gas phase volume fraction profiles.

Mass transfer between gas and liquid phases takes place in the whole systems (see Figure 9) according to Henry's law. It can be noticed that in static mixer reactor higher mass fraction of CO_2 dissolved in aqueous phase are achieved showing that its flow pattern and mixing characteristics promotes a higher interfacial area concentration and therefore a intensified mass transfer, while in CSTR reactor higher mass transfer rates are observed near to the impeller blades and even more at inlet reactor side.

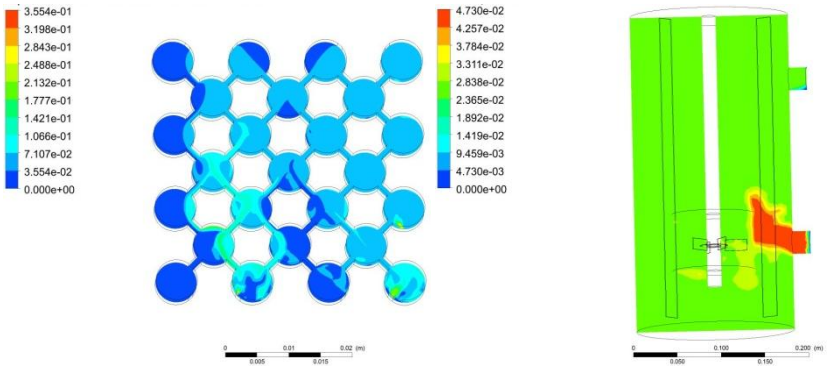

Figure 9. (a) NETmix® and (b) CSTR mass fraction of CO_2 dissolved in aqueous phase profiles.

4.3 THREE PHASES TWO COMPONENTS SYSTEM:

Once mass transfer mechanism was successfully implemented in model, the next step was to evaluate the hydrate formation based on the proposed stoichiometry (R.1). The applied boundary conditions set the system to operate with 3x excess of water mass flow.

According to the mass fraction of CO_2 dissolved in aqueous phase and solid phase volume fraction (Figure 10) it can be noticed that dissolved CO_2 is encaged by water molecules almost instantaneously in the network, forming the hydrate phase, which is carried by the flow upwards. The static mixer flow pattern promotes the mass transfer between gas and aqueous phase due to intensified mixing time and since the hydrate formation kinetic assumed for the model is fast, gas molecules are readily available to form hydrate phase. On the other hand, the CSTR flow pattern is less efficient promoting micro-mixing and the mass transfer between gas and aqueous phase resulting in lower concentration of CO_2 dissolved in water, what in turns reduces the formation rate of hydrates which is mixing controlled (see Figure 11).

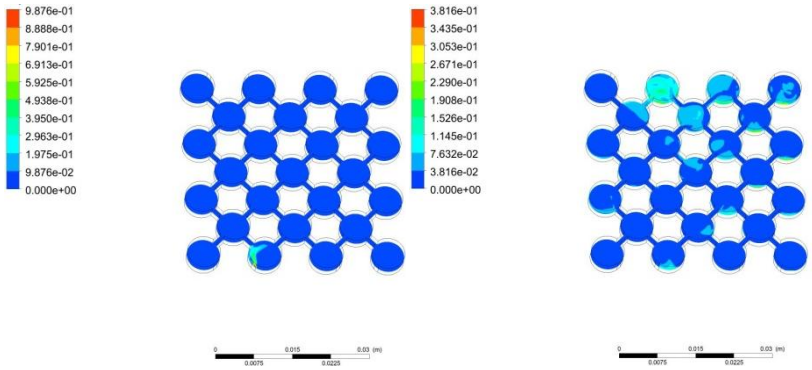

Figure 10. NETmix® (a) mass fraction of CO_2 dissolved in aqueous phase and (b) solid phase volume fraction profiles.

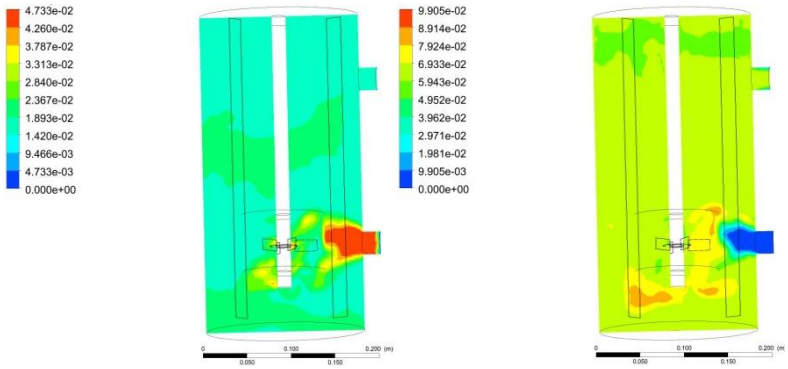

Figure 11. CSTR (a) mass fraction of CO_2 dissolved in aqueous phase and (b) solid phase volume fraction profiles.

5. CONCLUSION

This micro-reactor in complex net connections have short diffusion paths so it is avoided the analysis of radial mixing. This net mixing strategy acts as a static mixer, so increasing flow rates or pressure drops to create turbulence are not a strategy to mixing at this scale as is the case for CSTR reactor. The micro-mixing, or molecular mixing, is important to promote gas hydrate formation, and can be defined for turbulent flow regime as $\lambda_B = {}^{\eta}/_{\sqrt{Sc}}$ or as $\lambda_B = \left({}^{D_{AB}}/_{\nu}\right)^{-1/2}\left({}^{\nu^3}/_{\varepsilon}\right)^{1/4}$, where the Kolmogorov scale is more reliable in meso-mixing so it is more comprehensible to consider its calculation as $\eta = \left({}^{\nu^3}/_{\varepsilon}\right)^{1/4}$. For the static mixer due to laminar flow regime this analysis is based on Damkoehler number (Da), which relates the reaction rate with dissipation rate defined as $Da = k\left(\frac{Y_l^{CO_2}\rho_l\alpha_l}{MW_{CO_2 l}}\right)t_{mixing}$ and has shown that the hydrate formation rate is mixing driven. Obviously the macro-mixing in the channel is analyzed under Re. The CFD analysis shows that the chambers itself have almost few micro-mixing function (but reaction function to promote gas hydrate formation) and the complex interconnected channels as static mixers have mixing scales to be analyzed.

6. ACKNOWLEDGEMENTS

The work was conducted with the support of the ANP (National Petroleum Agency), ISPG and Petrogal Brasil S.A.

7. REFERENCES

ANSYS Fluent Theory Guide, ANSYS, Inc., 275 Technology Drive Canonsburg, PA 15317, Release 2019 R3.

Antal, S. P., Lahey, R. T., Flaherty, J. E., 1991. “Analysis of phase distribution in fully developed laminar bubbly two-phase flow”. International Journal of Multiphase Flow. 17. 5., 635–652.

Chatti, I., Delahaye, A., Fournaison, L., Petitet, J.-P., 2005. “Benefits and drawbacks of clathrate hydrates: a review of their areas of interest”. Energy Conversion and Management 46, 1333–1343.

Costa, M. F., Fonte C. M., Dias, M. M., Lopes, J. C. B., 2017. “Heat Transfer Performance of NETmix-A Novel Micro_Meso Structured Mixer and Reactor”. AIChE Journal 63, 2497-2508.

Drew, D. A., Lahey, R. T., 1993. In Particulate Two-Phase Flow. Butterworth-Heinemann. Boston, MA509–566.

Fonte, C. M., Leblebici, M., E., Dias, M. M., Lopes, J., C., B., 2012. “The Netmix® Reactor: 3d CFD Modelling and Pressure Drop Measurements”. In *Proceedings of the 14th European Conference on Mixing 2012*. Warsaw, Poland.

Gidaspow, Bezburuah, R., Ding, J., 1992. "Hydrodynamics of Circulating Fluidized Beds, Kinetic Theory Approach". In *Fluidization VII, Proceedings of the 7th Engineering Foundation Conference on Fluidization*. 75–82.

Hammerschmidt, E.G., 1934. “Formation of gas hydrates in natural gas transmission lines”. Industrial and Engineering Chemistry 26, 851–855.

Hibiki, Ishii, M., 200. "One-group Interfacial Area Transport of Bubbly Flows in Vertical Round Tubes". International Journal of Heat and Mass Transfer. 43. 2711–2726.

Laranjeira, P., E., Martins, A., A., Lopes, J., C., B., Dias, M., M., 2009. “NETmix® , A New Type of Static Mixer: Modeling, Simulation, Macromixing, and Micromixing Characterization”. AIChE Journal V.55 No. 9.

Legendre, D., Magnaudet, J., 1998. “The Lift Force on a Spherical Bubble in a Viscous Linear Shear Flow”. J. Fluid Mech. 368, 81–126.

Li, P., Zhang, X., Lu, X., 2019. “Three-dimensional Eulerian modeling of gas-liquid-solid flow with gas hydrate dissociation in a vertical pipe”. Chemical Engineering Science 196, 145-165.

Li, P., Zhang, X., Lu, X., 2019. “Three-dimensional Eulerian modeling of gas–liquid–solid flow with gas hydrate dissociation in a vertical pipe”. Chemical Engineering Science 196, 145–165.

Lun, C. K. K. , Savage, S. B. , Jeffrey, D. J., Chepurniy, N., 1984. "Kinetic Theories for Granular Flow: Inelastic Particles in Couette Flow and Slightly Inelastic Particles in a General Flow Field". J. Fluid Mech. 140. 223–256.

Mork, M., Gudmundsson, J., 2002. “Hydrate Formation Rate in a Continuous Stirred Tank Reactor: Experimental Results and Bubble-to-Crystal Model”. In *Proceedings of the 4th International Conference on Gas Hydrates 2002*. Yokohama, Japan.

Ogunlade B., Heleen de Coninck, D., Loos, M., Meyer, L., 2005. “IPCC - Special report on carbon dioxide capture and storage”. Cambridge University Press, UK. pp 431.

Paul, E. L., Atiemo-Obeng, V. A., & Kresta, S., 2004. “Handbook of industrial mixing: Science and practice”. Hoboken, N.J: Wiley-Interscience (2004).

Ranz, W. E., Marshall, W. R., 1952. “Evaporation from Drops, Part I and Part II”. Chem. Eng. Prog. 48(4). 173–180.

Ribeiro, C.P., Lage P.L.C., 2008. “Modelling of hydrate formation kinetics: State-of-the-art and future directions”. Chemical Engineering Science 63, 2007 – 2034.

Schaeffer, D. G., 1987. "Instability in the Evolution Equations Describing Incompressible Granular Flow". J. Diff. Eq. 66. 19–50.

Schiller L., Naumann, Z.; "Z. Ver. Deutsch. Ing. 77 (1935), 318.

Sloan, E. D., Koh, C. A., 2007. “Clathrate Hydrates of Natural Gases”. Third Edition.

Syamlal, M., 1987. "The Particle-Particle Drag Term in a Multiparticle Model of Fluidization". National Technical Information Service, Springfield, VA. DOE/MC/21353-2373, NTIS/DE87006500.

Tu, J., Yeoh, G., Liu, Chaoqun, C. “Computational Fluid Dynamics (Third Edition) Chapter 4 - CFD Mesh Generation: A Practical Guideline”. 2018.

Whitman, W. G. Chem. Met. Eng. 29. (1923) 146.

8. RESPONSIBILITY NOTICE

The authors are the only responsible for the printed material included in this paper.